Research Article | Vol. 34, No. 15 / 27 Jul 2026 / Optics Express 28081

Optics EXPRESS

Modeling light propagation and amplification efficiency in highly multimode, Yb-doped fiber amplifiers

DARCY L. SMITH,[1,2,3,†,*] KABISH WISAL,[2,†] BAICHUAN HUANG,[2] STEPHEN C. WARREN-SMITH,[1,4] ORI HENDERSON-SAPIR,[1,3] HUI CAO,[2] DAVID J. OTTAWAY,[1,3] AND A. DOUGLAS STONE[2]

[1] *Institute for Photonics and Advanced Sensing (IPAS) and the School of Physics, Chemistry and Earth Sciences, Adelaide University, 5005 SA, Australia*
[2] *Department of Applied Physics, Yale University, New Haven, CT 06520, USA*
[3] *OzGrav - Australian Research Council Centre of Excellence for Gravitational Wave Discovery, Adelaide Node, SA, Australia*
[4] *Future Industries Institute, Adelaide University, Mawson Lakes, 5095 SA, Australia*
[†] The authors contributed equally to this work.
[*] *darcy.smith@adelaide.edu.au*

Abstract: Multimode fibers have been proposed for mitigating nonlinear effects in high-power fiber amplifiers, allowing for significant power scaling. Most previous studies on light propagation in fiber amplifiers focus on single-mode or few-mode fibers. Here we develop a tractable numerical model to simulate light propagation in narrowband, highly multimode fiber amplifiers, which takes into account gain saturation and spatial hole-burning, pump depletion, and mode-dependent gain. We consider a frequency domain, field-based model which incorporates both gain-induced mode coupling and amplified spontaneous emission (ASE) from first principles. Our analysis is applied to Yb-doped fibers, with a semi-quantitative analysis identifying regimes in which either spontaneous emission or ASE limits amplifier efficiency. Our model can be combined with existing models for various nonlinear effects, providing a useful tool for quantitatively studying nonlinearity mitigation and power scaling in multimode fiber amplifiers.

1. Introduction

High-power fiber lasers utilizing multi-stage amplifiers enable a compact platform to achieve ultra-high laser power [1–4]. This has created a potential for applications in both fundamental science such as in gravitational wave detection [5], and industrial applications such as in advanced manufacturing [6], LiDAR [7], and defense [8]. To fully realize this potential, further power scaling is required. This is primarily limited by various nonlinear effects such as stimulated Brillouin scattering (SBS) [9–11], transverse mode instability (TMI) [12–14], and possibly, in the future, Kerr-induced modulation instability [15,16]. The mitigation of SBS and TMI in fibers is an ongoing area of research closely related to the challenge of power scaling in fiber lasers. Specifically for amplifiers with narrow linewidth, a requirement for important applications such as coherent beam combination and LiDAR, mitigating both SBS and TMI has been difficult. Most previous approaches utilize single mode fibers (SMF), motivated primarily by the high beam quality afforded by the Gaussian-like fundamental fiber mode. As such, most of the modeling efforts in fiber amplifiers have focused on SMF [17–19].

In several recent theoretical and experimental studies it was shown that both SBS and TMI can be efficiently mitigated by coherent multimode excitation in highly multimode fibers (MMFs) [20–26]. It has also been shown that for coherent excitations, a diffraction limited focused output

#599153 https://doi.org/10.1364/OE.599153
Journal © 2026 Received 17 Mar 2026; revised 19 Jun 2026; accepted 2 Jul 2026; published 21 Jul 2026

beam can be obtained by shaping the wavefront at the input in both passive and active fibers [27–31]. This demonstrates that MMFs can provide a novel platform for mitigating nonlinearities and achieving significant power scaling in fiber amplifiers. Another reason for significant recent interest in MMFs has been to study the interplay between nonlinear effects and spatial degrees of freedom, such as in Kerr beam self-cleaning [32]. To study these nonlinear effects in MMF amplifiers quantitatively, an accurate numerical model of light propagation and gain-induced nonlinearities in fibers under arbitrary multimode excitations is necessary. In this work we provide a computational frequency-domain model of amplification of narrowband light in MMFs, which takes into account gain saturation, pump depletion and mode-dependent gain. Our model of MMF amplifiers can then be combined with models for various unwanted nonlinear effects such as SBS, TMI and Kerr-induced four wave mixing, allowing quantitative predictions.

As mentioned above, significant work has been done in modeling light amplification in SMF amplifiers. The physical origin of the amplification of light is stimulated emission as it propagates through an optically pumped gain medium, which typically consists of rare-earth elements such as, Yb, Er, etc. doped into a silica fiber. Numerical models of fiber amplifiers require solving the optical wave equation for the signal coupled to pump light through the gain medium. The local gain is computed from the spatially-varying population inversion by solving steady-state rate equations. A key assumption commonly used is that the transverse mode profile of the amplified signal within the fiber is constant. This reduces the problem to a set of one-dimensional differential equations describing the evolution of pump and signal power, along with the population inversion. This framework accurately models light propagation in SMF, however, it becomes inaccurate if light propagates in multiple fiber modes. In particular, it fails to capture mode coupling due to spatial hole burning, which generates rapid spatial variations in the local gain due to multimode interference and gain saturation.

To accurately model an MMF amplifier, light propagation needs to be considered in multiple transverse modes and modeled using field amplitudes (instead of intensities) to account for multimode interference. In addition, mode-dependent gain and loss, and mode coupling induced by the presence of the gain medium within the fiber core, must be considered. An intensity-based model for MMF amplifiers was developed in Ref. [33], and while it was suitable for the study of few-moded fiber amplifiers (as used in telecommunications applications), it could not be accurately extended to highly multimode fibers, as it neglected modal interference, hence leading to issues with accurately maintaining power conservation and calculating efficiency. An improved model, involving multimode field amplitudes, was presented in Ref. [34], however the scope of this work was also few-moded telecommunications fibers, not highly multimode fibers. Another interesting study, which modeled MMF amplifiers, involved numerical simulation of the nonlinear Schrödinger equation to describe nonlinear effects in MMF amplifiers [35]. Since both Refs. [34] and [35] involved broadband light they were computationally limited to few-moded fibers. Mathematically, the computational runtime for such models scales as $O(N_w N_o^2)$, where N_w is the number of frequency bins required and N_o is the number of modes [36].

For studying high-power *narrow-linewidth*, MMF amplifiers it is possible to develop an computationally tractable model for *highly multimode* excitations. Here we focus on this case, where the narrowband signal is amplified by a broadband and incoherent pump and accompanied by broadband amplified spontaneous emission (ASE). In addition, as long as the signal linewidth is significantly smaller than the gain bandwidth, it can be considered as single-frequency. Furthermore, speckle effects can be neglected for an incoherent pump source and broadband ASE. With these simplifications the computational runtime in our approach scales as $O(N_o^2 + N_w)$. Our assumptions about the signal, pump and ASE light are informed by the experimental configurations commonly used in high-power MMF amplifiers with quasi-monochromatic continuous-wave (CW) output.

Optics EXPRESS

We begin by presenting a comprehensive derivation of the coupled equations for the evolution of signal modal amplitudes, pump power and fractional upper-level population. We solve these equations numerically with a fourth order Runge-Kutta finite difference method. Initially, we ignore ASE, and only consider multimode signal growth along with the evolution of pump. Later, we generalize to a broadband model which incorporates ASE. We simulate a highly multimode fiber at 1064 nm signal wavelength with a Yb-doped gain medium. We present results for the total signal power, pump power, individual modal power, modal gain, spatial-hole burning, signal reabsorption and pump-signal conversion efficiency for the first time with a fully field-based, multimode model. Crucially, we incorporate the cross-gain terms resulting from spatially varying gain saturation and population inversion. These terms are required to accurately maintain energy conservation. Finally, after generalizing our model to include broadband ASE, we study output efficiency, evolution of the gain spectrum, and output beam profile as a function of signal power. Overall, our work contributes an important tool for studying multimode fiber amplifiers, which provides a promising new platform for instability-free ultra high laser power.

2. Multimode fiber amplifier model

2.1. Multimode signal growth equations

We begin by deriving growth equations for signal light propagating through an active MMF, which are then solved numerically. We decompose the signal light into a set of transverse eigenmodes, each a solution to the optical wave equation given the fiber geometry. Previously, in the development of intensity-based MMF amplifier models, it was assumed that each mode propagates and interacts with the gain medium as an independent channel [17,33]. However, this assumption is not accurate, and the error associated with such a model grows with the number of propagating modes. In our work, we do not make this assumption, but instead show that the amplitude equations for various modes are coupled by the presence of the spatially-dependent gain medium.

In this section, the coupled equations governing the evolution of each modal amplitude and the gain-induced inter-modal coupling are derived from first principles. It is possible to arrive at these equations by combining multiple results in published work such as Refs. [34,35]. However, a clear and comprehensive prior derivation is lacking, to our knowledge. As such, in this section our intent is both pedagogical, to fill this gap, and to reach a starting point for the numerical results provided in this paper.

We consider a rare-earth doped fiber amplifier pumped from the input end (co-pumping). Later we also treat pumping from the output end (counterpumping). A broadband, incoherent pump beam excites the rare-earth ions, creating a population inversion. A coherent multimode signal beam is injected into the fiber core and undergoes amplification through stimulated emission. The electric field for the signal $\mathbf{E}_s$ obeys the Helmholtz electromagnetic wave equation:

$$\left[\nabla^2 - \frac{n^2}{c^2}\frac{\partial^2}{\partial t^2}\right]\mathbf{E}_s = 0, \tag{1}$$

where, c is the speed of light in vacuum. n is the local refractive index, which takes the following form:

$$n(\mathbf{r}) = n_0(\mathbf{r}_\perp) + in_g(\mathbf{r}), \tag{2}$$

where $n_0(\mathbf{r}_\perp)$ is the refractive index profile of the fiber in the absence of active dopants, assumed translationally invariant, and $in_g(\mathbf{r})$ is the change in the index of refraction due to the presence of the gain medium. A cylindrical coordinate system is used with z being aligned with the fiber axis; $\mathbf{r}_\perp$ represents the combined coordinates (x, y) in the plane transverse to the fiber axis. The imaginary part represents the processes of absorption/emission provided by the gain medium (n_g is negative in regions and at frequencies where the pumping creates gain, and positive elsewhere).

Optics EXPRESS

The frequency-dependent change in the real part of n due to n_g as dictated by the Kramers-Kronig relations is neglected. This is because this term only redistributes power within the fiber modes, leaving amplifier behavior qualitatively unchanged. In addition, the specific value of change in the real part of the refractive index due to the gain medium is highly specific to a given fiber along with the environmental conditions. For similar reasons, we also neglect random variations in the refractive index profile due to fiber imperfections leading to linear mode coupling. Both of these effects can be incorporated in our formalism in a straightforward manner if needed, based on experimental characterization of the particular fiber of interest.

We assume that $n_g \ll n_0$, such that n^2 can be approximated as:

$$n^2 \approx n_0^2 + 2in_0n_g. \tag{3}$$

Additionally, we expand the electric field in terms of the guided modes of the fiber:

$$\mathbf{E}_s(\mathbf{r}) = \sum_m A_m(z)\boldsymbol{\psi}_m(\mathbf{r}_\perp)\exp[i(\beta_m z - \omega_0 t)], \tag{4}$$

where, ω_0 denotes the signal frequency, $A_m(z)$ denotes the modal amplitude, $\boldsymbol{\psi}_m(\mathbf{r}_\perp)$ denotes the transverse mode electric-field profile, and β_m denotes the propagation constant for the m^{th} mode. Each fiber mode satisfies the fiber modal equation given by [37],

$$\left[\nabla_T^2 + \left(\frac{n_0^2\omega_0^2}{c^2} - \beta_m^2\right)\right]\boldsymbol{\psi}_m = 0. \tag{5}$$

Here, ∇_T^2 is the transverse Laplacian. Substituting our expressions for n and $\mathbf{E}$ into Eq. (1), we obtain:

$$\left[\nabla^2 + \frac{n_0^2\omega_0^2}{c^2} + i\frac{2n_0n_g\omega_0^2}{c^2}\right]\sum_m A_m(z)\boldsymbol{\psi}_m(\mathbf{r}_\perp)\exp(i\beta_m z) = 0. \tag{6}$$

We split the Laplacian operator into its transverse and longitudinal components, apply the slowly varying envelope approximation, and utilize the modal eigenvalue equation given in Eq. (5), obtaining:

$$\sum_m 2i\beta_m\frac{\mathrm{d}A_m(z)}{\mathrm{d}z}\boldsymbol{\psi}_m(\mathbf{r}_\perp)\exp(i\beta_m z) = \frac{2in_0n_g\omega_0^2}{c^2}\sum_n A_n(z)\boldsymbol{\psi}_n(\mathbf{r}_\perp)\exp(i\beta_n z). \tag{7}$$

To isolate a single term corresponding to mode m on the left hand side (LHS), we take the inner product with $\boldsymbol{\psi}_m^*$ on both sides and integrate across the transverse cross-section of the fiber, leveraging the orthonormality of transverse fiber eigenmodes. With some rearrangement, this leads to:

$$\frac{\mathrm{d}A_m(z)}{\mathrm{d}z} = \frac{n_0\omega_0^2}{\beta_m c^2}\sum_n A_n(z)\exp[i(\beta_n - \beta_m)z]\int n_g(\mathbf{r}_\perp, z)\,\boldsymbol{\psi}_m^* \cdot \boldsymbol{\psi}_n\,\mathrm{d}\mathbf{r}_\perp\,. \tag{8}$$

It can be seen that the change in amplitude of mode m with respect to propagation along z depends on the amplitudes of all fiber modes. The reason for the coupling between various modal amplitudes is the presence of transverse spatial dependence in the refractive index $n_g(\mathbf{r}_\perp, z)$. If n_g were constant across the fiber cross-section, the integral on the right hand side (RHS) of Eq. (8) would become proportional to δ_{mn}, decoupling the growth for each modal amplitude. This is the assumption used in previous intensity-based models of MMF amplifiers, leading to inaccuracies. However in the presence of gain saturation, n_g depends on the local signal intensity, which in MMFs is highly speckled, leading to strong spatial variations in n_g. As such, a coupled treatment of the modal amplitudes is necessary for accurate and consistent results.

Next, we write n_g in terms of the signal gain coefficient $g(\mathbf{r})$ due to stimulated emission, which depends on the population inversion [38,39]:

$$2\kappa_0 n_g(\mathbf{r}) = g(\mathbf{r}) = \sigma_{e,s} N_2(\mathbf{r}) - \sigma_{a,s} N_1(\mathbf{r}), \tag{9}$$

where $\kappa_0 = \omega_0/c$, $\sigma_{e,s}$ and $\sigma_{a,s}$ represent the emission and absorption cross-section at the signal frequency, and N_2 and N_1 are the number volume density of active ions in the excited and ground state respectively. The above expression for n_g allows us to write the equation for modal amplitude evolution in the following form:

$$\frac{\mathrm{d}A_m(z)}{\mathrm{d}z} = \sum_n g_{mn}(z) A_n(z) \exp[i(\beta_n - \beta_m)z], \tag{10}$$

where

$$g_{mn}(z) = \frac{1}{2} \int \boldsymbol{\psi}_m^* \cdot \boldsymbol{\psi}_n \, g(\mathbf{r}_\perp, z) \, \mathrm{d}\mathbf{r}_\perp. \tag{11}$$

The above two equations describe the multimodal signal growth and their solution forms a major part of our model. In the above form, these equations have a rather straightforward interpretation. The amplitude growth in any mode depends linearly on the amplitudes in each mode, with a corresponding gain coefficient between any two modes g_{mn} depending on the overlap between the modal profiles and the local signal gain coefficient $g(\mathbf{r})$, which depends on the local population inversion as given by Eq. (9). In the case of linear gain, where g is approximately constant in space, the equation for each modal amplitude becomes independent, leading to exponential growth in power in each mode, as expected. However, in general, in high-power fiber amplifiers, the local population inversion depends substantially on the local signal and pump intensity, making the signal growth equations highly nonlinear. As a result, finding analytical solutions to the signal growth equations is not possible, except in some very special cases. As such, in our model, we solve the signal growth equations numerically using a finite difference method. Before proceeding to that solution, we need to describe how the local population inversion, characterized by N_1 and N_2, depends on the signal and the pump intensity.

2.2. Population inversion and pump depletion

In our model, we consider an MMF amplifier that is doped with a rare-earth metal such as Ytterbium (Yb) or Erbium (Er), which provides signal gain via stimulated emission. In general, these ions have three energy levels which participate in amplification, as well as additional energy levels which may participate in processes such as excited-state absorption or upconversion. It has been shown however that these three-level systems can be modeled as effectively two-level systems owing to a separation in time scales associated with various transition rates [17,40]. In all cases in this paper, the gain medium is treated as such a two-level medium. In the case that a gain medium has a level structure which requires a more complicated treatment, the modeling of population inversion can be generalized without needing to change the signal and pump evolution equations in our model.

For simplicity, we assume that the dopant ions are uniformly spread over the fiber core with density N_{tot}. These ions occupy either the lower or the upper energy level, with population densities N_1 and N_2, respectively, such that $N_1 + N_2 = N_{\mathrm{tot}}$. Stimulated transitions between these levels are facilitated by the presence of pump light at frequency ν_p and signal light at frequency ν_s. Following the derivation presented in Refs. [17,18,40], the density of ions in the upper level in the steady-state regime is given by:

$$N_2(\mathbf{r}_\perp, z) = N_{\text{tot}} \frac{\frac{\sigma_a(\nu_p)}{\sigma_a(\nu_p)+\sigma_e(\nu_p)} \frac{I_p(\mathbf{r}_\perp,z)}{I_{\text{sat}}(\nu_p)} + \frac{\sigma_a(\nu_s)}{\sigma_a(\nu_s)+\sigma_e(\nu_s)} \frac{I_s(\mathbf{r}_\perp,z)}{I_{\text{sat}}(\nu_s)}}{1 + \frac{I_p(\mathbf{r}_\perp,z)}{I_{\text{sat}}(\nu_p)} + \frac{I_s(\mathbf{r}_\perp,z)}{I_{\text{sat}}(\nu_s)}}, \tag{12}$$

where saturation intensity is given by

$$I_{\text{sat}}(\nu) = \frac{h\nu}{(\sigma_a(\nu) + \sigma_e(\nu))\tau}. \tag{13}$$

Here, $\sigma_a(\nu)$ and $\sigma_e(\nu)$ represent the absorption and emission cross-section at frequency ν, with $\nu = \nu_s$ denoting the signal frequency and $\nu = \nu_p$ denoting the pump frequency. Upper level population density N_2 depends on both the signal intensity I_s and the pump intensity I_p relative to the respective saturation intensities $I_{\text{sat}}(\nu_s)$ and $I_{\text{sat}}(\nu_p)$. Note that the saturation intensity depends on the energy of the pump or signal photon divided by the total absorption and emission cross-section and the upper level lifetime τ, the inverse of the spontaneous emission (SpE) rate. As written in Eq. (12) various terms in the denominator represent rates of both emission and absorption of the signal and the pump normalized to the rate of SpE. Similarly, the numerator consists of terms representing the relative rate of only the absorption of the pump and the signal. Overall, the ratio of the numerator (representing absorption) and the denominator (representing both absorption and emission) gives the steady state population of the upper level. A derivation of this steady-state population inversion equation is given in [40].

Given N_{tot} as a known parameter of the fiber, Eq. (12) can be used to calculate N_2 and N_1 at any point in the fiber core, if the signal intensity I_s and pump intensity I_p are known. The remaining quantities depend on material and optical constants. The signal intensity $I_s(\mathbf{r}_\perp, z)$ is calculated from a coherent sum of the fiber modes, given by

$$I_s(\mathbf{r}_\perp, z) = \left| \sum\nolimits_m A_m(z) \boldsymbol{\psi}_m(\mathbf{r}_\perp) \exp(i\beta_m z) \right|^2. \tag{14}$$

The steady state signal intensity along with the inversion can be used to determine the quantum defect heating which is responsible for TMI. Thus our model can be easily integrated with a multimode TMI model [23] to calculate TMI threshold taking into account full gain saturation. We have highlighted an example of this calculation borrowed from our recent work on TMI modeling in multimode fibers [23] in Section 3 of Supplement 1.

Most standard fiber amplifiers are cladding-pumped, in which a broadband pump is launched into the pump core (the fiber inner cladding + core), while the dopant ions which absorb the pump are present only in the core. As the pump source is usually a spectrally incoherent diode launched into the many cladding modes, its speckle pattern ‘smears out’, and its transverse spatial profile over the fiber core can be assumed as constant. The pump intensity is then given as $I_p(z) = P_p(z)/A_{\text{cl}}$, where $P_p(z)$ is the total pump power at location z along the fiber axis and A_{cl} is the area of the inner cladding. Although the pump intensity is constant across the fiber cross-section, it varies significantly in the longitudinal direction, as the pump power decreases along the fiber axis due to pump absorption, usually referred to as pump depletion. Based on the rate equations, the evolution of pump power is given by [40]:

$$\frac{\mathrm{d}P_p(z)}{\mathrm{d}z} = -\frac{P_p(z)}{A_{\text{cl}}} \int [\sigma_{a,p} N_1(\mathbf{r}_\perp, z) - \sigma_{e,p} N_2(\mathbf{r}_\perp, z)] \mathrm{d}\mathbf{r}_\perp. \tag{15}$$

The pump power decreases exponentially along the fiber, with a variable rate depending on the local upper and lower level population.

Optics EXPRESS

2.3. Numerical solution approach

To summarize, our model consists of amplitude growth equations for the individual modal amplitudes of the signal (Eqs. 10) and (11)), and a single equation describing pump power depletion (Eq. (15)), coupled by a nonlinear steady state formula for the local population inversion (Eq. (12)). Together these equations fully describe the coherent amplification of a narrowband multimode signal in the presence of dopant ions excited by broadband, transverse spatially uniform pump light. One major effect we have not considered in this section is ASE, which can also extract energy from the pump. This will be discussed in Section 3.

Since the equations for the signal, population inversion and the pump are coupled and nonlinear, solving them analytically is not possible. To overcome this, we develop a numerical scheme for solving these equations based on the finite-difference method. Our algorithm can be summarized as follows. At the fiber input, we are given a pump power $P_p(z=0)$ and a multimode signal, represented by a set of complex modal amplitudes $A_m(z=0)$. The transverse mode profiles $\boldsymbol{\psi}_m$ and propagation constants β_m are calculated and stored for the given fiber. Assuming all the relevant material and optical constants are known, the goal is to calculate the signal, pump and population inversion throughout the fiber, i.e., obtain $A_m(z)$, $P_p(z)$, and $N_2(\mathbf{r}_\perp, z)$. This is achieved as follows.

Say at a point z, $A_m(z)$ and $P_p(z)$ are known, then we calculate $N_2(\mathbf{r}_\perp, z)$ using Eq. (12). With N_2 (and $N_1 = N_{\text{tot}} - N_2$), we calculate the local signal gain g_{mn}, providing the value of the RHS in Eq. (10) and Eq. (15). By discretizing the derivative on the LHS in Eq. (10) and Eq. (15), we update the value of $A_m(z+\Delta z)$ and $P_p(z+\Delta z)$ using the value of variables and derivatives at the previous steps. In this manner, we continue to iterate forward along the length of the fiber until $z = L$, alternating between calculating N_2 using the signal and pump intensity and updating the signal amplitudes and the pump power at the next step using the signal gain and pump absorption obtained from N_1 and N_2. The precise rule for updating depends on the discretization scheme employed. In our case, we considered both the Euler method and a fourth-order Runge-Kutta method. For sufficiently small Δz, both methods were able to produce accurate and consistent results. In general, Runge-Kutta provides higher accuracy but the Euler method requires less computational runtime, in accordance with the previous literature. The results presented in this work used the Runge-Kutta.

As the scale of variation along the variable of integration (z) is set by the longitudinal speckle grain size, which is constant along the length of the fiber, adaptive step-size techniques were not considered and rather a fixed step-size algorithm was used. This fixed step-size Δz was determined by considering the smallest longitudinal speckle-based feature size, given by $L_{\text{speckle}} = 2\pi/(\beta_{\max} - \beta_{\min})$, and suitably resolving this feature with at least 20 longitudinal points. The number of points per speckle was chosen through convergence testing, whereby doubling the resolution produced a change in output signal power of less than 0.2%. A similar convergence test was used to determine the transverse mesh, which contained an 80×80 grid in cylindrical coordinates, extending radially to twice the core radius. While an adaptive mesh size could have been used to improve runtime for less-moded fibers, this was not employed, as the main computational hurdle in the model was found to be the number of modes, and with a constant mesh discretization, less-moded fibers ran in negligible times compared to fibers of $\sim$ 100µm core diameter or larger.

2.4. Results of the single-frequency MMF amplifier model

The parameters used for the Yb-doped MMF amplifier are given in Table 1, representing realistic parameters for a 24-mode amplifier (including both polarizations), and the results are shown in Fig. 1. The relevant parameters of Ytterbium are given in Table 2. The steady-state pump and signal power as a function of z is presented in Fig. 1(a). The pump power decreases as the pump is absorbed and the signal power grows by extracting energy from the gain medium, as expected.

Optics EXPRESS

The signal power curve is comprised of a sum of each individual mode's power evolution, shown in Fig. 1(b). The multimode speckle of the signal and the resulting transverse population inversion distribution are shown at three points along the fiber in Fig. 1(c), demonstrating the progression from a highly excited to a depleted gain medium, as well as the transverse spatial hole burning induced by the multimode speckle.

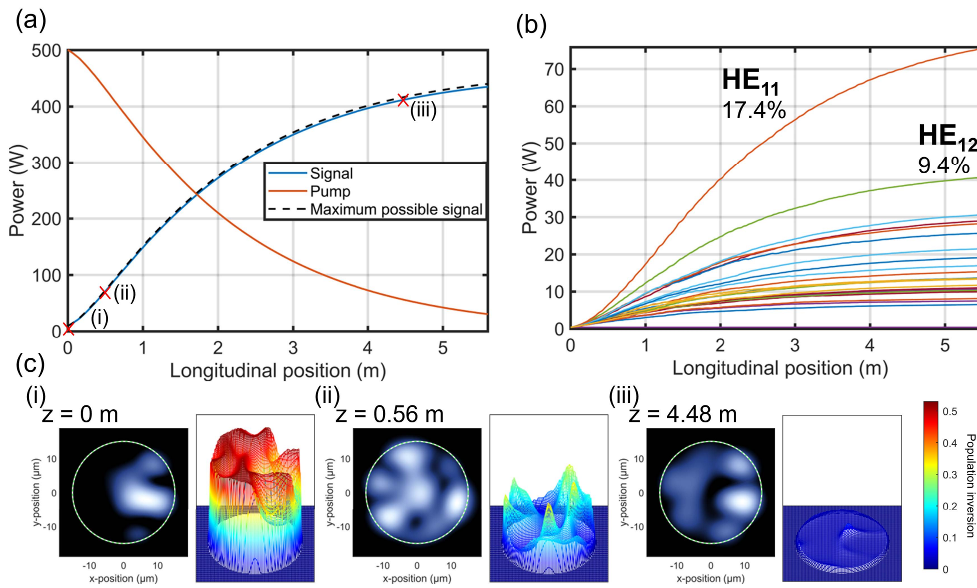

Fig. 1. Results of the multimode fiber amplifier model. 500 W of pump power and 10 W of signal power, distributed evenly amongst the 24 supported modes (accounting for the two polarizations corresponding to each propagation constant), are launched into the fiber described in Table 1. (a) Signal and pump power as a function of z. The maximum possible signal, as set by the Stokes efficiency, is displayed with the dashed line. (b) Power carried by each individual mode as a function of z. The two modes with the largest power output have been labeled along with the percentage of the total output signal power which they carry. (c) Transverse multimode speckle pattern (2D plot on left) and resulting population inversion (3D mesh plot on right) at (i) $z = 0$ m, (ii) 0.56 m and (iii) 4.48 m (indicated on (a)).

Table 1. Parameters of the fiber used to produce the results in Figs. 1 and 2

Parameter	Value
Core diameter (μm)	30
Cladding diameter (μm)	420
Core refractive index	1.447
Cladding refractive index	1.445
Core Yb population density (m^{-3})	10^{26}
Fiber length (m)	5.6
Signal wavelength (nm)	1064
Pump wavelength (nm)	975
Number of supported modes	24

Table 2. Relevant parameters of ytterbium

Parameter	Value
$\sigma_{a,s}$ (m^2)	5.52×10^{-27}
$\sigma_{e,s}$ (m^2)	3.27×10^{-25}
$\sigma_{a,p}$ (m^2)	2.21×10^{-24}
$\sigma_{e,p}$ (m^2)	2.1×10^{-24}
τ (s)	9.01×10^{-4}
λ_s (nm)	1064
λ_p (nm)	975

The two modes which extract the most power from the gain medium, along with the percentage of the total output signal power which they carry, are shown in Fig. 1(b). These two modes are the HE_{11} (fundamental) mode, and the HE_{12} mode. It is intuitive that the fundamental mode carries the most power out of the set of modes; it has the largest fraction of its power within the core [37], and its near-Gaussian shape ensures it is the most resilient against hole burning effects. The second most powerful mode, the HE_{12}, is less intuitive, but it shares a couple of properties with the HE_{11} mode which allow it to extract a relatively large amount of gain from the gain medium. Firstly, the HE_{1m} modes are the only vector modes with nonzero intensity at the center of the core, leaving a gain reservoir which only they draw from. Secondly, they are the only modes not part of a near-degenerate modal family, which can produce long beat-lengths and oscillatory gain competition, something the HE_{1m} modes are free from.

While the total signal power evolution shown in Fig. 1(a) and even the modal power evolution in Fig. 1(b) are relatively smooth, the gain experienced by each mode exhibits a strongly noisy oscillatory pattern as exemplified by the four representative modes in Fig. 2(a) and the full modal set of zoomed-in gain curves in Fig. 2(b). This is due to a combination of two multimode effects - the effect of speckle on the population inversion at a given z (as predicted in Eq. (12) and exhibited in Fig. 2(c)), and the individual overlap of each mode with this resulting population inversion which induces coupling between modes (as predicted in Eq. (11) and exhibited in Fig. 2(d)). As the population inversion is influenced by the multimode speckle, which shows longitudinal oscillatory behaviour stemming from the modal beating between every possible pair of propagating modes, so too do these longitudinal spatial frequencies ($f_{\text{beat}} = \Delta\beta/2\pi$) contribute to the oscillatory behavior shown in Fig. 2(a) and (b). Distinct modal beat frequencies are visible in the modal gain curves of few-moded fibers, but when the number of modes reaches ten or higher, the result is a seemingly stochastic (yet inherently deterministic) oscillation, with an overall envelope determined by the pump and signal powers, and deviations from this determined by the superposition of a large number of pairwise modal beats.

It can be seen from Fig. 1 that at all points in the fiber, the total signal power is less than the 'maximum possible signal power', defined as

$$P_{S,\max}(z) = P_s(0) + \eta_{\max}[P_p(0) - P_p(z)], \tag{16}$$

where the Stokes efficiency ($\eta_{\max}$) is defined as λ_p/λ_s. $P_{S,\max}(z)$ gives the signal power at a point z in the fiber if every pump photon absorbed up to that point resulted in a coherently produced signal photon through stimulated emission. As the signal transition is of a lower energy than the pump transition, this is less than 100% of the absorbed pump, with the remaining energy going into the quantum defect heating. Thus the maximum possible signal power is set by the Stokes efficiency, which for the pump and signal wavelengths used here is ~ 92%. All quoted efficiencies in this paper will be relative to $\eta_{\max}$, and hence it is important to note that efficiencies must be multiplied by $\eta_{\max}$ to convert them to pure optical efficiency (such as slope efficiencies

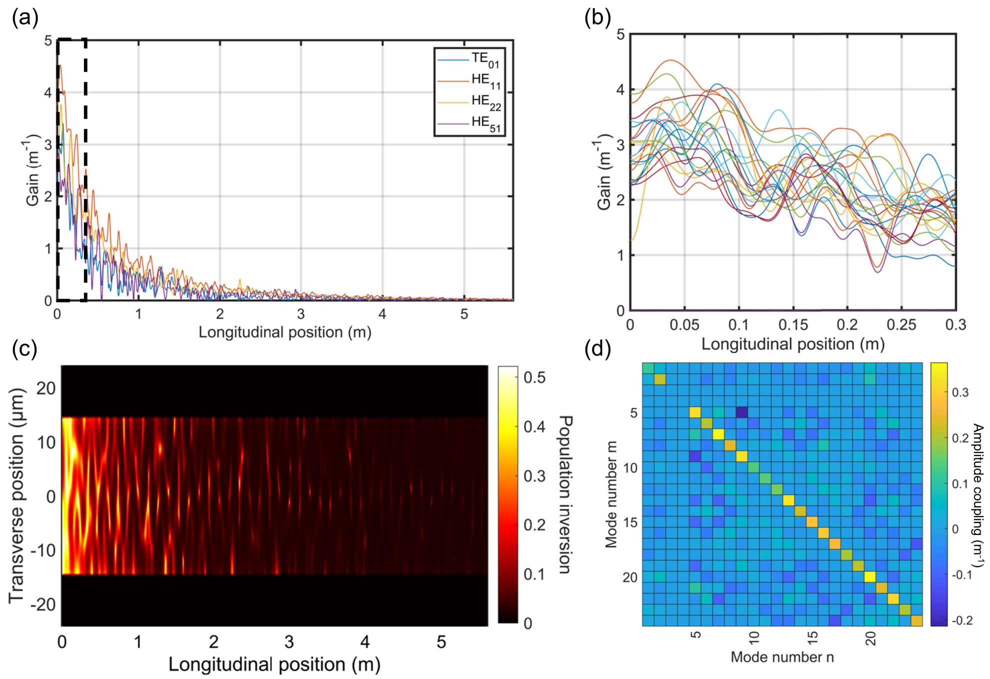

Fig. 2. (a) Modal gain as a function of z for four selected modes from the fiber described in Table 1. (b) Modal gain for all 24 supported modes of the fiber, zoomed-in to the inset section of (a). (c) Slice of the population inversion along the $x-z$ plane. (d) The g_{mn} matrix, as defined in Eq. (11), at $z = 5.6$ m.

quoted in experimental works). Although our current work focuses on theoretical derivation and numerical results of our MMF amplifier model, this model was validated experimentally in our recent work on SBS in a high-power MMF amplifier [31]. We have presented an example result of this validation in Section 2 of Supplement 1.

The Stokes efficiency only represents the upper limit on amplifier efficiency. Beyond the power lost through non-radiative energy dissipation, power is also lost through isotropically emitted spontaneous emission (SpE), due to the finite metastable state lifetime τ. In addition, the small fraction of the SpE emitted into guided modes is amplified, leading to broadband ASE, which competes with the signal for pump power and reduces the amplifier efficiency. The modeling of ASE is more complicated as it occurs everywhere within the fiber and can be guided in the backwards as well as forward direction. The explicit effect of ASE on the amplifier behavior will be discussed in detail in Section 3.1. However, qualitative analyses on regimes of amplifier behavior as it is limited by SpE and ASE can be made by studying the expression for population inversion given in Eq. (12).

We can rewrite Eq. (12) in the form:

$$N_2 = N_{\mathrm{tot}} \frac{f_a^p S_p/\tau + f_a^s S_s/\tau}{\left(\frac{1}{\tau} + \frac{S_p}{\tau} + \frac{S_s}{\tau}\right)}, \tag{17}$$

Optics EXPRESS

where f_a^p, f_a^s are the absorption cross-sections for the pump and signal, normalized by the total cross-section and S_p, S_s are the pump and signal intensities normalized to their saturation values:

$$f_a^i = \frac{\sigma_a(\nu_i)}{\sigma_a(\nu_i) + \sigma_e(\nu_i)}$$
$$S_i(\mathbf{r}) = \frac{I_i(\mathbf{r})}{I_{\text{sat}}(\nu_i)} \tag{18}$$
$$\text{where } i = s, p.$$

Note that we have multiplied by the spontaneous emission rate, $1/\tau$, in numerator and denominator. One sees that in principle both strong pumping and strong signal contribute to the population inversion. However, for Yb, $f_a^p \approx 1/2$, while $f_a^s \sim 10^{-2}$, and I_{sat} is roughly ten times lower for the pump than for the signal. While the cladding radius is often an order of magnitude larger than the core radius, it is almost always the case that the input pump power is 1-2 orders of magnitude larger than the input signal power. Hence, within the pump depletion length, the pump term in the numerator of Eq. (17) dominates. Furthermore, the rate of SpE generation is generally proportional to population inversion. The signal is limited in the inversion it can generate alone due to its negligible absorption cross-section, hence the region of the fiber where SpE most strongly affects gain/efficiency is within the pump absorption length, where the pump term will generally be at least an order of magnitude larger than the signal term. Therefore, parameters which determine amplifier efficiency such as population inversion and the rate of stimulated emission relative to spontaneous emission are mainly determined by the pump saturation. S_p, S_s, and N_2 vary in space and need to be calculated in order to model the amplifier, but we will neglect this effect for the current qualitative arguments.

First, as the emission cross-section at the signal frequency is much greater than the absorption cross-section, the system can have gain when $N_2 \approx (\sigma_{a,s}/\sigma_{e,s})N_1 \ll N_1$ (see the expression for gain given in Eq. (9)). In this limit $N_{\text{tot}} \approx N_1$ and since f_a^p is order unity, the pump does not need to be saturated for the amplifier to have relatively weak gain. When this is the case, the first term in the denominator, representing SpE, will dominate over the second and third terms, and most of the energy from the pump will be dissipated through SpE. As SpE is emitted isotropically, very little of this emission is coupled into the fiber, and little pump power is converted into either signal or ASE guided within the fiber. Therefore it is necessary to saturate the pump at the input to have a useful amplifier. This is indeed the case in most experimental configurations involving high-power fiber amplifiers.

When the pump is saturated ($S_p \gg 1$), but the seed is too weak, then the signal will not be saturated near the input ($S_s \ll 1$). In this case the second (pump absorption) term in the denominator dominates, yielding $N_2 \sim N_1$, and the gain will approach its maximum possible value. SpE will still represent an important loss mechanism, as it occurs more often than stimulated emission of the signal (third term in the denominator) near the input. Moreover, as already noted, the small fraction of SpE which couples into the guided modes of the amplifier can be amplified by the pump as ASE. However, ASE will only be dominant over SpE near the input when this fraction, $2\Delta\Omega/4\pi \sim 10^{-3} > S_s$ (where $\Delta\Omega$ is the solid angle subtended by the guided modes - see Eq. S.24). For Yb, we find that this only occurs for a relatively weak seed $\sim 10 - 100$ mW. At higher seed powers, in the range 100 mW$-$1 W, we find that ASE can still compete for gain with the signal and significantly reduce amplifier efficiency. Once S_s exceeds $\sim$10, the effect of ASE becomes negligible. The effect of ASE on efficiency is studied in detail in Section 3.1, confirming the estimates given here.

Finally, when both pump and signal are saturated ($S_p, S_s \gg 1$), most of the pump energy will be converted to amplification of the signal and the amplifier will operate near its maximum possible efficiency over the pump depletion length. Thus it is important to ensure that the seed is strong enough to saturate the signal for efficient operation, particularly in the multimode case

Optics EXPRESS

where large core sizes result in lower intensity for a given power, and unsaturated speckle enables ASE and self-lasing.

The effect of SpE on amplifier efficiency is demonstrated in Fig. 3(a), beginning with a 10 µm core diameter and 50 µm cladding diameter fiber with 1 kW pump, 30 W signal and sufficient length to absorb 95% of the pump. The core and cladding diameter is increased up to 200/1000 µm, while keeping either the intensity constant or the total power constant. Dopant density N_{tot} is scaled with $1/r_{\text{co}}^2$ such that the total dopant number stays constant, and hence the pump absorption length remains similar across simulations. The number of excited modes is restricted to 20 for each core size supporting more - this is done both for consistent simulation lengths and longitudinal resolution requirements, and to avoid loss of efficiency from sources other than SpE such as mode-dependent loss near the cutoff and spatial hole burning effects. The initial modal power distribution is selected by simulating the launching of an off-axis Gaussian beam, and selecting the 20 modes with the largest coupled power launched into them. This modal power distribution is then renormalized to the nominal input signal power. This method provides a balance between controlled simulation conditions and realistic experimental launching. The input signal is sufficient to suppress ASE in all cases, isolating SpE as the efficiency loss mechanism.

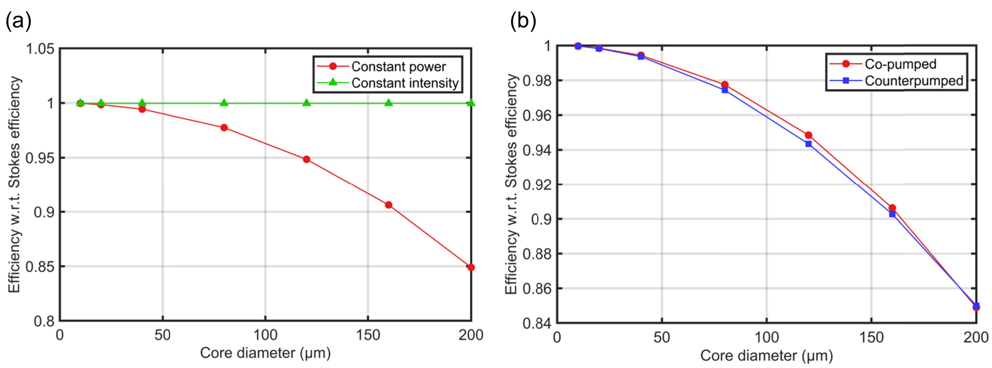

Fig. 3. (a) Amplifier efficiency with respect to the Stokes efficiency as a function of core diameter (with the cladding diameter scaled by a constant factor of the core diameter - here $d_{\text{cl}} = 5d_{\text{co}}$). Nominal power is defined as 1 kW input pump and 30 W input signal at 10 µm core diameter, with constant intensity demanding this power is increased as per the square of the core size increase. Dopant density is scaled as $1/d_{\text{co}}^2$ such that the dopant number remains constant as core size is changed. In this way, the pump absorption length remains similar for all cases. The first 20 modes of each fiber are chosen for fibers supporting more than 20 modes. (b) Amplifier efficiency with respect to the Stokes efficiency for the cases of co- and counterpumping, with parameters otherwise the same as the red curve in (a).

Since scaling at constant intensity leaves the pump and signal saturation constant, as expected, the efficiency remains constant at almost 100%. However, when the total power is kept constant, the signal intensity decreases below saturation and SpE begins to degrade the efficiency significantly. The constant-power scaling reduces both the saturation of the signal and pump substantially, but up to the largest core size the pump remains saturated, so the main effect on efficiency comes from the decrease in the stimulated emission rate and hence increase in spontaneous emission rate relative to this.

This decrease in amplifier efficiency with increasing core size due to SpE is an effect which becomes increasingly relevant as the power-scaling potential of multimode fibers is pursued. Cladding-pumped fibers with large cladding sizes require very high pump power to strongly saturate the gain. If pump power is fixed then a large seed power can compensate with its own contribution to saturation, but for Yb this is highly inefficient and would require impractically large seed powers (see Section 3.2).

Figure 3 (b) presents results similar to the red curve in (a), this time comparing a co- and counterpumped amplifier. These cases correspond to the input of the pump from $z = 0$ (i.e. propagating with the signal) and $z = L$ (i.e. propagating against the signal) respectively. The modeling of a counterpumped amplifier is performed using the shooting method [41], the details of which are discussed in Section 4a of Supplement 1.

For Fig. 3(b), other than the pumping configuration, we have used the same parameters as Fig. 3(a). In all cases the input signal is sufficiently saturating the gain and suppressing ASE, hence any decrease in efficiency is due to SpE and insufficient pump saturation. The results demonstrate that the difference in efficiency between these configurations is negligible, with the counterpumped case producing an efficiency less than 1% smaller on average than that of co-pumped. Hence, when the input signal is sufficiently saturating the gain, there is no advantage or disadvantage to co- or counterpumping an MMF amplifier from an efficiency point of view. A description of the modeling of forwards and backwards propagating ASE in the co- and counterpumped cases is presented in Section 4B of Supplement 1.

3. Broadband MMF amplifier model

In the previous section, both pump and signal light were considered as single-frequency. However, for many fiber amplifier applications, such as the study of nonlinear pulse propagation [35,42] or wavelength-multiplexed telecommunications [43,44], the spectrally-dependent and broadband nature of the light propagating through the fiber becomes significant and even crucial. Furthermore, ASE is an inherently broadband process which can interfere with intended amplifier behavior, regardless of whether the signal light of interest is narrow-linewidth or not. In this section, a broadband MMF amplifier model is presented, which takes into account the spectrally-dependent nature of rare-earth dopants, again focusing specifically on Yb.

3.1. Details of the broadband model

In the presence of broadband light, the response of the gain medium can be given as

$$N_2(\mathbf{r}) = \frac{R_a(\mathbf{r})}{R_a(\mathbf{r}) + R_e(\mathbf{r}) + 1/\tau} N_{\mathrm{tot}}(\mathbf{r}), \tag{19}$$

where

$$R_i(\mathbf{r}) = \int \frac{1}{h\nu}\sigma_i(\nu) I(\mathbf{r},\nu)\mathrm{d}\nu \tag{20}$$

are the spectrally integrated absorption and emission contributions to the overall population inversion. By expressing the light as two delta-functions in frequency at ν_p and ν_s, Eq. (19) reduces to Eq. (12). For high-power, single-frequency amplifier operation, it remains reasonable to assume such single-frequency dependence for the pump and signal. However, ASE remains inherently broadband, and Eqs. (19) and (20) are required to describe its effects on amplifier operation. Furthermore, one may wish to model the signal as a finitely narrow source, exploring the spectral evolution of its lineshape, making it necessary to give the signal spectral width.

For the below results, the pump is assumed to be spatially incoherent over the core. Spectrally, it is represented by an effective center frequency ν_p, which is adequate when the pump bandwidth is narrow compared with the scale over which the Yb cross sections vary or when effective cross sections are used. The signal and ASE exist over a discrete set of evenly-spaced wavelengths $\lambda_j = c/\nu_j$, each defining the center wavelength of a bin of width $\Delta\lambda$. This bin width is chosen so as to reasonably resolve the spectral cross-section curves shown in Fig. S5. With these assumptions regarding the optical channels being considered, Eq. (20) can now be expressed as

$$R_i(\mathbf{r}) = \frac{\sigma_{i,p}}{h\nu_p}\frac{P_p(z,\nu_p)}{A_{\mathrm{cl}}} + \int_\nu \frac{1}{h\nu}\sigma_i(\nu)I_{\mathrm{tot}}(\mathbf{r},\nu)\mathrm{d}\nu, \tag{21}$$

where $I_{\mathrm{tot}}(\mathbf{r},\nu) = I_s(\mathbf{r},\nu) + I_{\mathrm{ASE}}(\mathbf{r},\nu)$. In both converting from frequency to wavelength and converting from the continuous to discrete case, the integral in Eq. (21) can be expressed as following:

$$\frac{1}{hc}\sum_j \sigma_i(\lambda_j)I_{\mathrm{tot}}(\mathbf{r},\lambda_j)\lambda_j. \tag{22}$$

ASE is assumed to be broadband; it is generated at every frequency which has a non-zero emission cross-section. It is also generated everywhere within the pumped section of the fiber and propagates in both the forwards and backwards directions. Modeling backwards ASE requires using the self-consistent relaxation method; a discussion of our method for modeling backwards ASE (together with backwards propagating pump) is given in Section 4A of Supplement 1.

At each z-step, spontaneous emission (SpE) is generated due to the finite upper state lifetime of the active ions [40,45], according to Eq. (23) (derivation presented in Section 6 of Supplement 1):

$$\frac{\mathrm{d}P_{\mathrm{SE}}(z,\nu)}{\mathrm{d}z} = 4\pi^2\mathrm{NA}^2{r_{\mathrm{co}}}^2\frac{h\nu^3}{c^2}\sigma_e(\nu)\delta\nu\iint \mathrm{d}\mathbf{r}_\perp N_2(\mathbf{r})\hat{i}_{\mathrm{SE}}(\mathbf{r},\nu). \tag{23}$$

This expression for the generation of SpE deviates from that derived in [40] and used in [34,35] in that the expression for the capture solid angle of SpE emitted within the fiber considers the NA of the fiber, rather than a single-mode approximation which has been used thus far in literature. The result is an expression for $\mathrm{d}P_{\mathrm{SE}}(z,\nu)/\mathrm{d}z$ which is tailored for multimode optical fibers, and does not suffer from inaccuracies which scale with the number of guided modes in the fiber.

In Eq. (23), $\hat{i}_{\mathrm{SE}}$ describes the unit intensity profile which SpE takes while propagating. In previous works [34,35], it is assumed that SpE is coupled into fiber modes in an incoherent manner, that is, ASE modes add as intensities, not fields. However, as the ASE band is wide (from THz to 10s of THz), its spectral correlation time is orders of magnitude smaller than the modal group delay spread. This means relative modal phases for one frequency are decorrelated from adjacent frequencies within the ASE band, and for highly multimode fibers, the spatial profile becomes smeared out like the incoherent pump. Hence we assume that ASE takes a uniform transverse spatial profile. The SpE generated over a z step is added to the existing accumulation of SpE which has experienced amplification in the same way as the signal, and hence becomes ASE. Therefore, the growth of ASE throughout the fiber can be described by

$$\frac{\mathrm{d}P_{\mathrm{ASE}}(z,\nu)}{\mathrm{d}z} = 4\pi\mathrm{NA}^2\frac{h\nu^3}{c^2}\sigma_e(\nu)\delta\nu\iint N_2(\mathbf{r})\mathrm{d}\mathbf{r}_\perp + \frac{P_{\mathrm{ASE}}}{A_{\mathrm{co}}}\int[\sigma_e(\nu)N_2(\mathbf{r}) - \sigma_a(\nu)N_1(\mathbf{r})]\mathrm{d}\mathbf{r}_\perp. \tag{24}$$

Hence, Eqs. (19), (21) and (24), together with Eq. (10) evaluated at each wavelength λ_i and Eq. (15), describe the propagation of broadband, multimode light through the gain medium of a fiber amplifier.

3.2. Results of the broadband MMF amplifier model

In this section we evaluate the effect of ASE for Yb amplifiers using the broadband model. For Yb the main phenomenon is the suppression of ASE with increased input signal. For other rare-earth systems, such as Er, there are other spectral effects such as reabsorption of the signal, but we defer this analysis to future work. As alluded to in Section 2.4, sufficient signal saturation is required to suppress ASE. In general, the signal and ASE share the pump power which is not lost to isotropic SpE emission, and one can define a 'global' efficiency, which measures how efficiently pump power is converted into propagating light in the fiber. The global efficiency is mainly set by the level of pump saturation in relation to the SpE rate, and the signal saturation determines how this efficiency is shared amongst signal band channels (signal + ASE).

As discussed in Section 2.4, the normalized signal power can be expressed as $S_s = P_s/P_{\text{sat},s}$, where $P_{\text{sat},s} = A_{\text{co}} I_{\text{sat},s}$. For a saturated pump ($S_p$>>1) but weak signal, ASE is the main source of efficiency loss in an MMF amplifier. Figure 4 gives amplifier behavior as a function of S_s for a fiber with a core diameter of 50 µm, 1 kW of input pump, and parameters otherwise the same as in previous sections. Figure 4 (a) and (b) give the pump, signal, forwards and backwards ASE power as a function of position in the fiber for $S_s = 1$ and $S_s = 100$ respectively, demonstrating the general longitudinal characteristics of ASE and its suppression with increased signal power. Figure 4 (c) gives the output signal power and output ASE (forwards + backwards), as well as the total signal band power (signal + forwards ASE + backwards ASE) as a function of S_s, demonstrating the gain competition between signal and ASE, and the input signal required to suppress ASE.

As expected, increased signal power results in reduced ASE, with ASE becoming suppressed once S_s exceeds ~ 10. This is because the magnitude of SpE generation depends on the upper-state lifetime τ and S_p, two parameters which here are constant. Hence the relative magnitude of SpE generation depends only on the input signal. As such, the gain competition which ensues is also dependent only on signal input. The backwards propagating ASE serves to saturate the pump at the front of the fiber, and is suppressed at a similar rate with respect to input signal power as the forwards ASE.

Figure 4 (d) gives signal efficiency and global efficiency as a function of input signal power. The signal efficiency is defined as before, while, as noted above, the global efficiency considers all channels which are drawing power from the pump (signal + forwards ASE + backwards ASE), with the Stokes efficiency for ASE considering its centroid wavelength of ~1030 nm rather than 1064 nm for the signal.

In addition to demonstrating ASE suppression, Fig. 4(d) demonstrates that the global efficiency is set mainly by the level of pump saturation (given f_a^p>>f_a^s), as a high efficiency is possible without signal saturation. While the absorbed power is shared between signal and ASE, we find that the sum of power in channels across the signal wavelength band will reach roughly the same efficiency regardless of how it is partitioned. Secondly, although signal absorption (f_a^s) for Yb is small, it is still non-negligible, especially for large input signal powers. Thus, despite each datapoint in Fig. 4(d) having the same input pump power, there is a small increase of 1% in global efficiency due to the increase in input signal by four orders of magnitude from 10^{-1} to 10^3. This however is an incredibly inefficient method of increasing efficiency, and highlights the need for sufficient pump saturation.

Figure 5 gives the input signal required to reach 90% signal efficiency as a function of core diameter in the case that cladding diameter is increased proportionally to core diameter, and hence pump saturation decreases with core diameter. Larger core sizes require stronger input pump power to suppress loss due to SpE, while at smaller core sizes in which SpE is already suppressed, input signal power must be large enough to suppress ASE. As seen in Fig. 4, S_s dropping below ~ 10 generally allows ASE to compete for gain with the signal and decrease signal efficiency.

For Fig. 5, the cladding diameter is fixed such that $d_{\text{cl}} = 5d_{\text{co}}$. Hence with a constant pump input of 500 W, S_p decreases as ~ d_{co}^{-2}. For core diameters up to ~100 µm, this pump saturation is still sufficient to set the global efficiency above the 90% threshold by itself. In this regime, the signal power only needs to be strong enough to suppress ASE, hence being labeled the 'ASE limit' and only requiring small input signal powers relative to the pump power (~1 W). While it appears from Fig. 5(a) that the input signal required is steadily increasing exponentially across all core sizes, it can be seen that there is a slight change of slope at ~ 100 µm, denoting the

Optics EXPRESS

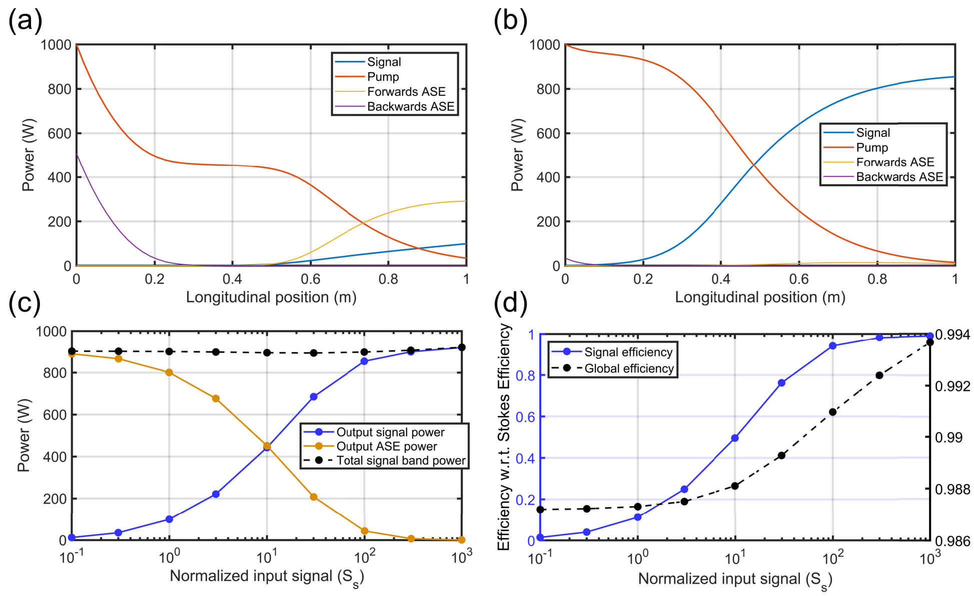

Fig. 4. Progression of pump power, signal power and backwards and forwards propagating ASE for a 50 µm core diameter Yb-doped fiber with 1 kW pump input. The input signal powers are (a) $P_s(0) = P_{\text{sat},s}(S_s = 1)$ and (b) $P_s(0) = 100P_{\text{sat},s}(S_s = 100)$, where S_s is the normalized signal power (as used in Eq. (17)). Here, $P_{\text{sat},s} = 14$ mW. (c) gives the output signal power ($P_s(L)$), output ASE power ($P_{\text{ASE},+}(L) + P_{\text{ASE},-}(0)$), and total signal band power (sum of the two) as a function of input signal power for otherwise constant fiber parameters. (d) gives the signal efficiency and global (total signal band) efficiency with respect to the Stokes efficiency as a function of the input signal power.

boundary between the amplifier being limited by ASE and SpE. This boundary is clear when considering signal saturation, expressed as S_s. In the ASE limit, the input signal saturation required to sufficiently suppress ASE and achieve 90% signal efficiency is relatively constant and slightly decreasing with increased core size (5(b)). Given the global efficiency for these core sizes is well above the 90% threshold, the partitioning of total power between signal and ASE is purely determined by the level of signal saturation. The decrease as a function of core size results from decreased SpE generation with decreased pump saturation as the core size increases, until the global efficiency falls below 90% and the SpE-limited regime is entered.

For core diameters greater than ~100 µm, the pump saturation is not sufficient to set the global efficiency above the 90% threshold on its own, hence both high signal power (5(a)) and high signal saturation (5(b)) are required to make up the global efficiency lost to SpE. Past the transition between the ASE and SpE limits at approximately $d_{co} = 100$ µm, the threshold input signal increases dramatically, due to the fact that $f_a^s << f_a^p$ for Yb, and hence unreasonably high signal powers are needed to set the amplifier efficiency at 90%.

These results highlight the need to consider pump and signal saturation levels when increasing fiber core size for reasons such as suppressing SBS or inducing higher order modes. While ASE suppression on its own only requires modest signal input powers and fixed saturation levels, SpE itself becomes a harsh limit in the case that pump saturation is not sufficient. Large signal powers in the 100s of W and above are required in such regimes, highlighting the need to dramatically increase pump power when entering the large core, multimode fiber amplifier regime.

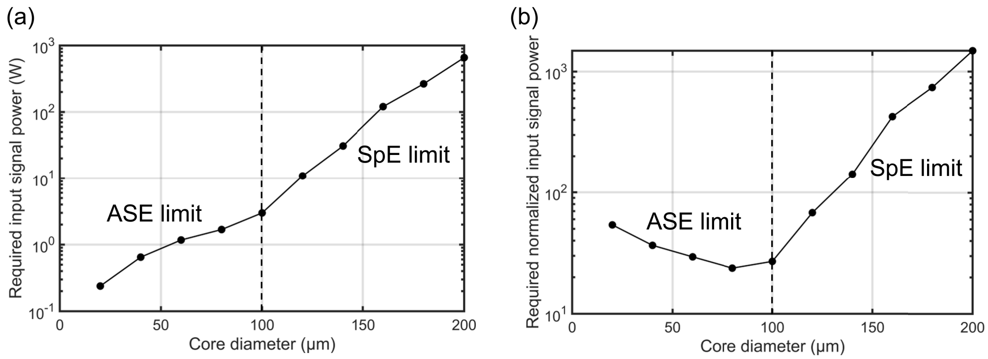

Fig. 5. (a) Input signal power and (b) signal power normalized to saturation power ($S_s = P_s/P_{\text{sat},s}$, where $P_{\text{sat},s} = A_{\text{co}}I_{\text{sat},s}$) required to reach 90% output signal efficiency at a length of 95% pump absorption as a function of core diameter. The cladding diameter is set to $5d_{\text{co}}$, hence for constant input pump power, the intensity and saturation decreases as $\sim d_{\text{co}}^{-2}$. The primary limits on amplifier efficiency for the regimes of small core, high pump saturation vs large core, low pump saturation are labeled as 'ASE limit' and 'SpE limit' respectively, with the delineation between them denoted with a vertical dashed line.

4. Discussion and conclusion

We have presented a derivation and analysis of a field-based MMF amplifier model, applicable to highly-multimode, high-power fiber lasers, an application of such a model as yet unexplored in the literature. The derivation in Section 2.1 allows insight and intuition into how the multimode character of the signal and noise in such amplifiers affects their properties and specifically their efficiency. In such systems the signal is typically narrowband, whereas the ASE noise is broadband, hence we have introduced both a 'single-frequency' system of equations for modeling the signal and SpE, and a broadband model with evolution equations appropriate to modeling ASE. Our formulation of this broadband model allows a computationally efficient treatment specific to the highly multimode regime, allowing us to analyze effects such as efficiency loss to ASE as a function of seed power, as well as the spectral shape of this ASE. The model is then applied to Yb-doped fiber amplifiers of varying core and cladding dimensions.

The single-frequency results depict modal gain and amplifier efficiency in the context of high-power Yb-doped fiber amplifier operation. Such fiber amplifiers are increasingly relevant for applications such as the generation/suppression of non-linear effects and wavefront shaping/beamshaping techniques. We find that such an amplifier can operate at a large fraction of its Stokes efficiency up to ~ 100 μm core diameter with a 500 W pump and 10 W seed. The pump will need to be stronger to have high efficiency beyond that core diameter. We show that a non-saturated pump can be somewhat compensated by a larger seed, but this is an inefficient and impractical approach for Yb. By employing our broadband model we show that power loss to ASE for Yb is a negligible effect for seeds above ~1 W. However this may not be the case for other dopants such as Er, where reabsorption of the signal is much stronger than in Yb. Our model suggests Er will have significant differences from Yb due to the differing spectroscopic characteristics between the two ions. Such effects are planned to be studied in future work.

Funding. Australian Research Council (FT200100154, CE230100016); United States Air Force Office of Scientific Research (FA-9550-20-1-0160).

Acknowledgments. The authors acknowledge and thank Linh V. Nguyen of the Future Industries Institute, Adelaide University, for his stimulating discussions and useful contributions to this work. Darcy Smith acknowledges the American Australian Association for the support of his research and thanks the Yale Quantum Institute for the use of their facilities.

Disclosures. The authors declare no conflicts of interest.

Data availability. Data underlying the results presented in this paper are not publicly available at this time but may be obtained from the authors upon reasonable request.

Supplemental document. See Supplement 1 for supporting content.

References

1. C. Jauregui, J. Limpert, and A. Tünnermann, "High-power fibre lasers," Nat. Photonics **7**(11), 861–867 (2013).
2. M. N. Zervas and C. A. Codemard, "High power fiber lasers: A review," IEEE J. Sel. Top. Quantum Electron. **20**(5), 219–241 (2014).
3. J. W. Dawson, M. J. Messerly, R. J. Beach, *et al.*, "Analysis of the scalability of diffraction-limited fiber lasers and amplifiers to high average power," Opt. Express **16**(17), 13240–13266 (2008).
4. J. Hecht, "High-power fiber lasers," Opt. Photonics News **29**(10), 30–37 (2018).
5. F. Wellmann, M. Steinke, F. Meylahn, *et al.*, "High power, single-frequency, monolithic fiber amplifier for the next generation of gravitational wave detectors," Opt. Express **27**(20), 28523–28533 (2019).
6. R. Carter, "From concept to industry: Ultrafast laser welding," Am. Ceram. Soc. Bull. **100**, 20–27 (2021).
7. J. Liu, X. Zhu, W. Diao, *et al.*, "All-fiber airborne coherent doppler lidar to measure wind profiles," EPJ Web Conf. **119**, 10002 (2016).
8. H. Kaushal and G. Kaddoum, "Applications of lasers for tactical military operations," IEEE Access **5**, 20736–20753 (2017).
9. G. P. Agrawal, *Nonlinear Fiber Optics* (Academic Press, 2019).
10. C. Wolff, M. J. A. Smith, B. Stiller, *et al.*, "Brillouin scattering—theory and experiment: tutorial," J. Opt. Soc. Am. B **38**(4), 1243–1269 (2021).
11. A. Kobyakov, M. Sauer, and D. Chowdhury, "Stimulated brillouin scattering in optical fibers," Adv. Opt. Photonics **2**(1), 1–59 (2010).
12. C. Jauregui, C. Stihler, and J. Limpert, "Transverse mode instability," Adv. Opt. Photonics **12**(2), 429–484 (2020).
13. A. V. Smith and J. J. Smith, "Mode instability in high power fiber amplifiers," Opt. Express **19**(11), 10180–10192 (2011).
14. M. N. Zervas, "Transverse-modal-instability gain in high power fiber amplifiers: Effect of the perturbation relative phase," APL Photonics **4**(2), 022802 (2018).
15. R. Dupiol, A. Bendahmane, K. Krupa, *et al.*, "Intermodal modulational instability in graded-index multimode optical fibers," Opt. Lett. **42**(17), 3419–3422 (2017).
16. G. P. Agrawal, P. L. Baldeck, and R. R. Alfano, "Modulation instability induced by cross-phase modulation in optical fibers," Phys. Rev. A **39**(7), 3406–3413 (1989).
17. C. Giles and E. Desurvire, "Modeling erbium-doped fiber amplifiers," J. Lightwave Technol. **9**(2), 271–283 (1991).
18. R. Paschotta, J. Nilsson, A. C. Tropper, *et al.*, "Ytterbium-doped fiber amplifiers," IEEE J. Quantum Electron. **33**(7), 1049–1056 (1997).
19. G. P. Agrawal, "Amplification of ultrashort solitons in erbium-doped fiber amplifiers," IEEE Photonics Technol. Lett. **2**(12), 875–877 (1990).
20. W.-W. Ke, X.-J. Wang, and X. Tang, "Stimulated brillouin scattering model in multi-mode fiber lasers," IEEE J. Sel. Top. Quantum Electron. **20**(5), 305–314 (2014).
21. C.-W. Chen, L. Nguyen, K. Wisal, *et al.*, "Mitigating stimulated brillouin scattering in multimode fibers with focused output via wavefront shaping," Nat. Commun. **14**, 7343 (2023).
22. K. Wisal, C.-W. Chen, Z. Kuang, *et al.*, "Optimal input excitations for suppressing nonlinear instabilities in multimode fibers," Optica **11**(12), 1663–1672 (2024).
23. K. Wisal, C.-W. Chen, H. Cao, *et al.*, "Theory of transverse mode instability in fiber amplifiers with multimode excitations," APL Photonics **9**(6), 066114 (2024).
24. K. Wisal, S. C. Warren-Smith, C.-W. Chen, *et al.*, "Generalized theory of sbs in multimode fiber amplifiers," in *Physics and Simulation of Optoelectronic Devices XXX* (SPIE, 2022), p. PC1199504.
25. K. Wisal, S. Warren-Smith, C.-W. Chen, *et al.*, "Theory of stimulated brillouin scattering in fibers for highly multimode excitations," Phys. Rev. X **14**(3), 031053 (2024).
26. C.-W. Chen, K. Wisal, Y. Eliezer, *et al.*, "Suppressing transverse mode instability through multimode excitation in a fiber amplifier," Proc. Natl. Acad. Sci. U. S. A. **120**(22), e2217735120 (2023).
27. R. Florentin, V. Kermene, J. Benoist, *et al.*, "Shaping the light amplified in a multimode fiber," Light: Sci. Appl. **6**(2), e16208 (2017).
28. S. Rothe, K. Wisal, C.-W. Chen, *et al.*, "Output beam shaping of a multimode fiber amplifier," Opt. Commun. **577**, 131405 (2024).
29. A. D. Gomes, S. Turtaev, Y. Du, *et al.*, "Near perfect focusing through multimode fibres," Opt. Express **30**(7), 10645–10663 (2022).
30. C.-W. Chen, K. Wisal, M. Fink, *et al.*, "Output control of dissipative nonlinear multimode amplifiers using spacetime symmetry mapping," Nat. Phys. **21**(5), 839–845 (2025).
31. S. Rothe, C.-W. Chen, P. Ahmadi, *et al.*, "Wavefront shaping enables high-power multimode fiber amplifier with output focus," Science **390**(6769), 173–177 (2025).
32. K. Krupa, A. Tonello, B. M. Shalaby, *et al.*, "Spatial beam self-cleaning in multimode fibres," Nat. Photonics **11**(4), 237–241 (2017).

33. Q. Kang, E.-L. Lim, Y. Jung, *et al.*, “Accurate modal gain control in a multimode erbium doped fiber amplifier incorporating ring doping and a simple lp01 pump configuration,” Opt. Express **20**(19), 20835–20843 (2012).
34. J.-B. Trinel, G. Le Cocq, Y. Quiquempois, *et al.*, “Theoretical study of gain-induced mode coupling and mode beating in few-mode optical fiber amplifiers,” Opt. Express **25**(3), 2377–2390 (2017).
35. Y.-H. Chen, H. Haig, Y. Wu, *et al.*, “Accurate modeling of ultrafast nonlinear pulse propagation in multimode gain fiber,” J. Opt. Soc. Am. B **40**(10), 2633–2642 (2023).
36. L. G. Wright, Z. M. Ziegler, P. M. Lushnikov, *et al.*, “Multimode nonlinear fiber optics: Massively parallel numerical solver, tutorial, and outlook,” IEEE J. Sel. Top. Quantum Electron. **24**(3), 1–16 (2018).
37. A. Snyder and J. Love, *Optical Waveguide Theory* (Springer US, 1983).
38. A. Siegman, *Lasers* (University Science Books, 1986).
39. E. Hecht, *Optics* (Pearson Education, Incorporated, 2017).
40. E. Desurvire, *Erbium-Doped Fiber Amplifiers* (Wiley, 2002).
41. M. Osborne, “On shooting methods for boundary value problems,” Journal of Mathematical Analysis and Applications **27**(2), 417–433 (1969).
42. R. Lindberg, P. Zeil, M. Malmström, *et al.*, “Accurate modeling of high-repetition rate ultrashort pulse amplification in optical fibers,” Sci. Rep. **6**(1), 34742 (2016).
43. N. Bergano and C. Davidson, “Wavelength division multiplexing in long-haul transmission systems,” J. Lightwave Technol. **14**(6), 1299–1308 (1996).
44. C. Brackett, “Dense wavelength division multiplexing networks: principles and applications,” IEEE J. Select. Areas Commun. **8**(6), 948–964 (1990).
45. H. Kogelnik and A. Yariv, “Considerations of noise and schemes for its reduction in laser amplifiers,” Proc. IEEE **52**(2), 165–172 (1964).